FULL PAPER

Diffuse Scattering

ADVANCED
OPTICAL
MATERIALS

www.advopticalmat.de

Coding Metasurfaces for Diffuse Scattering: Scaling Laws, Bounds, and Suboptimal Design

Massimo Moccia, Shuo Liu, Rui Yuan Wu, Giuseppe Castaldi, Antonello Andreone, Tie Jun Cui,* and Vincenzo Galdi*

Coding metasurfaces, based on the combination of two basic unit cells with out-of-phase responses, have been the subject of many recent studies aimed at achieving diffuse scattering, with potential applications to diverse fields ranging from radar-signature control to computational imaging. Here, via a theoretical study of the relevant scaling-laws, the physical mechanism underlying the scattering-signature reduction is elucidated, and some absolute and realistic bounds are analytically derived. Moreover, a simple, deterministic suboptimal design strategy is introduced that yields results comparable with those typically obtained by approaches based on brute-force numerical optimization, at a negligible fraction of their computational burden, thereby paving the way to the design of structures with arbitrarily large electrical size. Results are corroborated by rigorous full-wave numerical simulations and microwave experiments, and may be of interest in a variety of application fields, such as the design of low-scattering targets and illumination apertures for computational imaging, not necessarily restricted to electromagnetic scenarios.

1. Introduction

Driven by the seminal work by Yu et al.,[1] metasurfaces have gained considerable momentum, and nowadays constitute one of the most promising research thrusts in the field of artificial materials. By leveraging the concepts of radio-frequency "reflect array"[2] and "transmit array"[3] antennas, and expanding their applicability to terahertz and optical wavelengths, metasurfaces enable the precise control and local tailoring of an electromagnetic wavefront (in terms of amplitude, phase,

Dr. M. Moccia, Prof. G. Castaldi, Prof. V. Galdi
Fields & Waves Lab
Department of Engineering
University of Sannio
I-82100 Benevento, Italy
E-mail: vgaldi@unisannio.it
Dr. S. Liu, R. Y. Wu, Prof. T. J. Cui
State Key Laboratory of Millimeter Waves
Southeast University
Nanjing 210096, China
E-mail: tjcui@seu.edu.cn
Prof. A. Andreone
Department of Physics
University of Naples "Federico II," and CNR-SPIN
I-80125 Naples, Italy

and/or polarization) via the engineering of metallic or dielectric resonating elements suitably arranged on a 2D surface. Indeed, their inherent 2D character has played a major catalyzing role, by considerably simplifying the fabrication process, as opposed to "bulk" 3D metamaterials.[4] The reader is referred to refs. [5–9] (and references therein) for recent reviews on the modeling, design, and attainable physical effects, as well as the abundant applications, ranging from wavefront shaping and beam-forming to chemical and biological sensing.

Of specific interest for the present study is the concept of "coding and digital" metasurfaces, recently put forward by Cui et al.[10] (see also ref. [11] for an analogous concept applied to bulk metamaterials), which relies on the exploitation of a limited number of element-types (unit cells). In its simplest form, only two element-types (labeled as "1" and "0") are employed, so that the metasurface design can be effectively associated with a 2D binary coding. This can be viewed, in a sense, as an evolution of the "checkerboard-surface" concept originally conceived by Paquay et al.[12] As implied by the name, the basic idea underlying a checkerboard surface is to alternate two types of unit cells (e.g., metallic and artificial-magnetic-conducting, at microwave frequencies) characterized by out-of-phase reflection coefficients, so as to suppress the specular reflection in view of the inherent cancellation effects. With suitable extensions and modifications of the unit cells as well as the spatial arrangement, this basic concept has been exploited in several subsequent studies[13–18] in order to attain broadband and wide-angle reduction of the radar cross-section (RCS) of planar surfaces.

Within this framework, the digital-metasurface concept[10] introduces further levels of sophistication. First, the spatial arrangement (described by a coding) of the unit cells is far more general and flexible. Further versatility can be introduced by employing more than two unit cells, corresponding to multibit coding. Most important, by exploiting reconfigurable unit cells (whose response can be switched, e.g., by means of a biased diode or a microelectromechanical system), the coding is no longer irreversibly bound to the structure design, but can be controlled, e.g., via a field-programmable gate array. To date, this represents one of the first working examples of a programmable metamaterial platform for field manipulation and

processing and has stirred a considerable interest during the past couple of years. The reader is referred to refs. [19–38] for a representative (but nonexhaustive) sample of recent studies on digital metasurfaces. Among the most prominent applications, besides the aforementioned RCS control, particularly worth of mention are those to field shaping in reverberating scenarios,[19] computational imaging,[26] and dynamic control of polarization, wavefront and scattering signature,[33] as well as of information entropy.[31] Interestingly, some of these results and applications have recently been extended to acoustic scenarios.[39,40]

The present study focuses on coding metasurfaces for diffuse scattering. With specific reference to the binary case, it was shown in ref. [10] that the coding could be optimized in such a way that the scattered field due to an impinging plane wave would be distributed uniformly among all possible directions. By comparison with simple checkerboard geometries,[12–18] this implies a considerable reduction in both the monostatic and bistatic RCSs of the metasurface, and also finds important applications to computational imaging. Starting from these results, our study here addresses two important open issues that are inherently related to the numerical optimization. First, since there is no guarantee that a numerical optimization algorithm can reach the global optimum (in view of the inherently non-quadratic nature of the objective function), we theoretically study the scaling law of the RCS reduction and derive some bounds that allow assessing the "goodness" of an optimized coding. Second, since brute-force numerical optimization rapidly becomes computationally unaffordable for electrically large metasurfaces, we derive a simple, deterministic coding strategy which, by comparison against the aforementioned bounds, turns out to be suboptimal. This suboptimal coding will provide results that are comparable with that obtained via brute-force optimization, and can be applied to

arbitrarily large metasurfaces, with a negligible computational burden.

2. Background Theory and Modeling

2.1. Idea and Geometry

Figure 1 illustrates the basic idea and geometry of the coding metasurfaces under investigation, as well as the Cartesian (x, y, z) and associated spherical (r, θ, ϕ) coordinate systems utilized throughout. More specifically, Figure 1a conceptually schematizes a binary-coding metasurface, as in ref. [10]. We assume a planar structure, in the $x - y$ plane, featuring two possible element types, labeled with "1" and "0," implemented in turn as "supercells" consisting of square arrangements of $M \times M$ identical unit cells (shown in Figure 1b,c, respectively). There are several possible choices of the unit cells, which result in different characteristics in terms of frequency, angular, and polarization sensitivity. To facilitate direct comparison with the optimized-coding results in ref. [10], we consider the same unit-cell geometry (see Figure 1d), consisting of a square metallic patch of sidelength w laid on a grounded dielectric substrate of relative permittivity ε_r and thickness h. Accordingly, letting a the unit-cell period, the supercell total sidelength is $d = Ma$, while the total metasurface sidelength is Nd. The "1" and "0" element-types are implemented via suitable choices of the patch sidelength (w_1 and w_0, respectively), so that the corresponding reflection phases differ by 180° at the design frequency. The proper choice of all parameters (including the number M of unit cells per linear dimension) will be detailed hereafter.

As previously mentioned, and conceptually illustrated in Figure 1e, the aim of this study is to suitably synthesize a
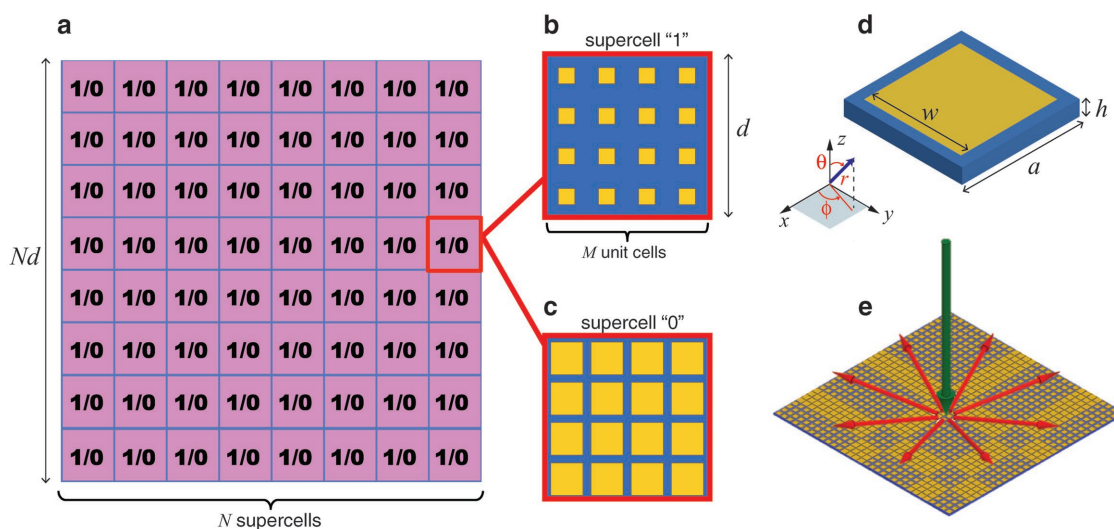
Figure 1. Illustration of the idea and geometry. a) Conceptual illustration of a binary-coding metasurface, comprising a square arrangement of $N \times N$ elements (represented as magenta squares) of two possible types (labeled with "1" and "0"). b,c) Schematics of the supercells implementing the "1" and "0" element types, respectively. Each supercell consists of a square arrangement of $M \times M$ identical unit cells, with total sidelength d. d) Geometry of the unit cell (of period $a = d/M$). The "1" and "0" element types are implemented via suitable choices of the patch side length (w_1 and w_0, respectively), so that the corresponding reflection coefficients are out of phase at the design frequency. Also shown are the Cartesian (x, y, z) and associated spherical (r, θ, ϕ) coordinate systems utilized throughout. e) Conceptual illustration of the diffuse scattering: a normally incident plane wave (thick green arrow) is scattered uniformly in all possible directions (thinner red arrows).

coding to realize diffuse scattering, so that a normally incident plane wave (thick green arrow) is scattered in all possible directions (thinner red arrows) in the most uniform fashion.

2.2. Semianalytical Modeling

In what follows, we study the scattering properties of our coding metasurfaces for plane-wave illumination (normally impinging along the negative z-direction), with suppressed $\exp(-i\omega t)$ time-harmonic dependence. As a meaningful observable to quantify the scattering signature, we consider the bistatic RCS[41]

$$\sigma(\theta,\phi) = \lim_{r \to \infty} 4\pi r^2 \frac{|\boldsymbol{E}_s|^2}{|\boldsymbol{E}_i|^2} \tag{1}$$

where $\boldsymbol{E}_i$ and $\boldsymbol{E}_s$ denote the incident and scattered electric fields, respectively, and (θ, ϕ) indicates an observation direction in the far region. Here, and henceforth, boldface symbols are used to indicate vector quantities. To compactly parameterize the diffuse-scattering properties of our coding metasurfaces, it makes sense to normalize the RCS with respect to that of a reference, a perfectly electric conducting (PEC) target of same size, and to eliminate the direction-dependence by considering the worst-case scenario (maximum-scattering direction) for both targets. Accordingly, we define the RCS ratio as

$$\gamma = \frac{\max\limits_{\theta,\phi} \sigma_{MS}(\theta,\phi)}{\max\limits_{\theta,\phi} \sigma_{PEC}(\theta,\phi)} \tag{2}$$

where the subscripts "MS" and "PEC" identify the metasurface and PEC targets. For the reference PEC planar scatterer, the maximum RCS is observed at the specular direction, which, for the assumed normal incidence corresponds to backscattering ($\theta = 0$). In Equation (2), and henceforth, the observation directions are restricted to the upper-half space ($z > 0$), i.e., $0 \le \theta \le \pi/2$, $0 \le \phi \le 2\pi$. Rigorous computation of the observable in Equation (2) requires the full-wave numerical solution of two 3D scattering problems, as detailed below. Nevertheless, we also consider a semianalytical approximation that was developed in ref. [10] (see also the Supporting Information for details)

$$\gamma \approx \frac{\lambda^2}{4\pi A} \max_{\theta,\phi} D(\theta,\phi) \tag{3}$$

with $\lambda = 2\pi c/\omega$ denoting the vacuum wavelength (and c the corresponding speed of light), A the (identical) area of the targets, and

$$D(\theta,\phi) = \frac{4\pi |\boldsymbol{f}(\theta,\phi)|^2 |F(k\sin\theta\cos\phi, k\sin\theta\sin\phi)|^2}{\displaystyle\int_0^{2\pi} d\phi \int_0^{\pi/2} d\theta \sin\theta |\boldsymbol{f}(\theta,\phi)|^2 |F(k\sin\theta\cos\phi, k\sin\theta\sin\phi)|^2} \tag{4}$$

the metasurface "directivity." The expression in Equation (4) closely resembles the directivity of antenna arrays.[41] In particular, we identify the "supercell factor"

$$\boldsymbol{f}(\theta,\phi) = \left(\hat{\boldsymbol{y}}\cos\theta - \hat{\boldsymbol{z}}\sin\theta\sin\phi\right)$$
$$\times \mathrm{sinc}\left(\frac{kd\sin\theta\cos\phi}{2}\right) \mathrm{sinc}\left(\frac{kd\sin\theta\sin\phi}{2}\right) \tag{5}$$

and the "array factor"

$$F(k_x, k_y) = \sum_{n,l=0}^{N-1} \Gamma_{nl} \exp\left[-id(nk_x + lk_y)\right] \tag{6}$$

with $\hat{\boldsymbol{\alpha}}$ denoting an α-directed unit vector, $\mathrm{sinc}(x) \equiv \sin(x)/x$, $k = 2\pi/\lambda$ the vacuum wavenumber, N the number of supercells per linear dimension (see Figure 1a), Γ_{nl} the reflection coefficient associated with the generic supercell (centered at $x_n = nd$, $y_n = ld$), and k_x and k_y the x- and y-domain wavenumbers, respectively.

The semianalytical approximation in Equations (4)–(6) provides an insightful working model, which is instrumental in the following developments. Its accuracy will be assessed by comparison against full-wave numerical simulations.

2.3. Numerical Modeling

The semianalytical model in Equations (4)–(6) is numerically implemented via an in-house Python code (www.python.org). The metasurface design and cross-validation rely also on rigorous full-wave simulations by means of the finite-element-based commercial software package Ansys HFSS (Electromagnetics suite Release 16.2.0, www.ansys.com/Products/Electronics/ANSYS-HFSS). The geometrical and constitutive parameters utilized are detailed hereafter in the various examples. Further implementation details are available in the Supporting Information.

3. Results and Discussion

3.1. Optimized Coding

Several brute-force optimization strategies have been proposed in order to design coding metasurfaces with minimized RCS, including hybrid,[20] particle-swarm,[23] simulated annealing,[27] and genetic[35] algorithms. In this study, as a benchmark, we consider the optimized-coding results obtained in ref. [10] (based on hybrid optimization as in ref. [20]). The corresponding 1D coding sequences are reported in Table S1 (Supporting Information), together with the corresponding RCS reductions, for various lengths. The same coding sequence is assumed for the two directions, so that the 2D coding is readily obtained via dyadic product of the 1D sequence by itself. The optimization is specifically intended for a structure featuring unit cells (see Figure 1d) of period $a = 7$ mm, with patch sidelengths $w_1 = 3.75$ mm and $w_0 = 4.8$ mm, for the "1" and "0" element-types, respectively; a substrate of thickness $h = 1.964$ mm is assumed, with $\varepsilon_r = 2.65$, $\tan\delta = 0.001$, and copper metallization of thickness 18 μm. The full-wave-computed reflection-phase responses pertaining to the two element-types are shown in Figure S1 (Supporting Information) as a function of the
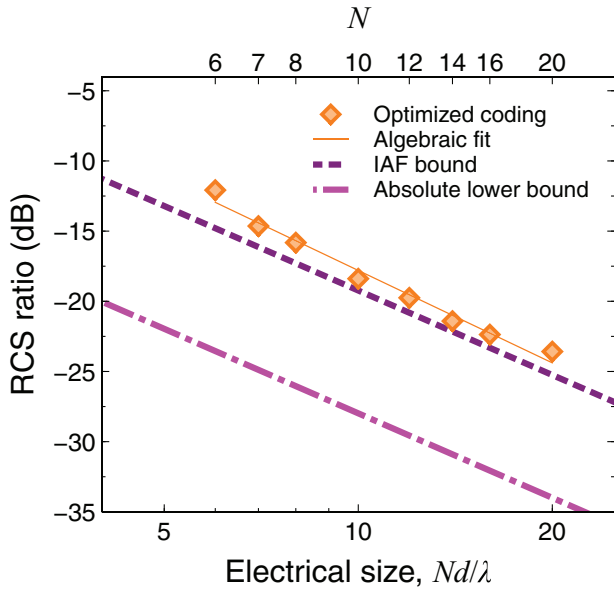
Figure 2. Optimized-coding versus derived bounds. The RCS ratio (orange-diamond markers) is plotted as a function of the metasurface electrical size on a log-log scale. The corresponding number N of supercells (of sidelength $d = \lambda$) per linear dimension is shown on the top axis. Also shown, as references, are the algebraic fit (Equation (7); orange-solid line), as well as the absolute (Equation (13); magenta-dashed-dotted line) and IAF (Equation (16); purple-dashed line) bounds. The optimized-coding sequences and corresponding RCS ratios are extracted from ref. [10] and, for convenience, are also reported in Table S1 (Supporting Information). Results specifically refer to a unit cell of period $a = 7$ mm, with patch sidelengths $w_1 = 3.75$ mm and $w_0 = 4.8$ mm, for the "1" and "0" element-types, respectively; a substrate of thickness $h = 1.964$ mm is assumed, with $\varepsilon_r = 2.65$, $\tan \delta = 0.001$, and copper metallization of thickness 18 μm. The operational frequency is 8.57 GHz.

frequency. It can be observed that the two responses are almost out of phase over a rather broad bandwidth, and the phase difference is exactly 180° at 8.7 GHz and 11.5 GHz. The optimized-coding metasurfaces is obtained by arranging (according with the 2D coding pattern) supercells made of 7×7 unit cells, with a total sidelength $d = 49$ mm. The nominal design frequency is chosen as 8.57 GHz, i.e., very close to the 180°-phase-difference condition. We observe that, at this frequency, the supercell sidelength is exactly one wavelength ($d = \lambda$).

Figure 2 shows the RCS ratio (orange-diamond markers) pertaining to the above optimized-coding metasurfaces as a function of their electrical size (or, equivalently, the number of supercells per linear dimension). A linear decreasing trend is observable which, in view of the log–log scale utilized, is qualitatively indicative of an algebraic scaling law. For a more quantitative assessment, the numerical algebraic fit

$$\gamma_{\text{fit}} \approx 2.552 \left(\frac{\lambda}{Nd}\right)^{2.187} \approx \frac{32.08\lambda^{2.187}}{4\pi A^{1.0935}} \tag{7}$$

is superimposed (orange-solid line). In the second approximate equality of Equation (7), we have explicitly substituted the metasurface area $A = (Nd)^2$, and have factored out a 4π term. This allows a more direct and insightful comparison with the semianalytical approximation in Equation (3). In what follows,

we will elucidate the physical nature and implications of such scaling law. This will allow us to address two crucial aspects that remain unresolved in view of the inherent limitations of brute-force numerical optimization. First, since the RCS is a complicated function of the reflection-phase distribution (cf. Equations (2)–(6)), with many local minima, there is no guarantee that the results in Figure 2 are close to the "global optimum." Therefore, in principle, there could be room for further reduction, e.g., in terms of a faster algebraic decay or a smaller multiplicative constant. Second, in view of the rapid growth of the computational burden with the electrical size, the optimized results in Figure 2 are necessarily limited up to moderately large structures ($A = 20\lambda \times 20\lambda$). Thus, different routes should be explored in order to render the RCS minimization of very large metasurfaces computationally affordable.

3.2. Scaling Laws and Bounds on RCS Reduction

By comparing the optimized-coding scaling-law numerical fit in Equation (7) with the semianalytical approximation in Equation (3), we note that, apart from slight differences (<10%) in the exponents, the two expressions exhibit the same structure, thereby indicating that the maximum directivity of the metasurface is essentially independent of its electrical size. This represents a pivotal observation, since it elucidates the physical mechanism underlying the RCS reduction and its scaling law. In essence, the diffuse scattering induced by the optimized coding maintains the metasurface maximum RCS constant, irrespective of its electrical size. Since the RCS of the reference PEC target is instead proportional to its electrical area, the RCS ratio scales as $\sim \lambda^2/A$.

Based on the above observation, we can derive some theoretical bounds to the RCS reduction. First, in view of the assumed coordinate-separable coding (with identical sequences along the two dimensions), the array factor in Equation (6) can be further factored as

$$F(k_x, k_y) = \Lambda(k_x)\Lambda(k_y) \tag{8}$$

thereby effectively reducing the study to a 1D array factor

$$\Lambda(\kappa) = \sum_{n=0}^{N-1} \Gamma_n \exp(-ind\kappa) \tag{9}$$

with Γ_n denoting the reflection coefficient associated with the generic supercell, whose element-type is dictated by the n-th bit of the 1-D coding sequence. Accordingly, the metasurface directivity in Equation (4) becomes

$$D(\theta, \phi) \approx \frac{4\pi|f(\theta,\phi)|^2|\Lambda(k\sin\theta\cos\phi)|^2|\Lambda(k\sin\theta\sin\phi)|^2}{\int\limits_0^{2\pi}d\phi\int\limits_0^{\pi/2}d\theta\sin\theta|f(\theta,\phi)|^2|\Lambda(k\sin\theta\cos\phi)|^2|\Lambda(k\sin\theta\sin\phi)|^2} \tag{10}$$

A first bound can be derived by finding the condition under which the maximum value (with respect to θ and ϕ) of the metasurface directivity is minimized. Intuitively, this happens in the perfectly "isotropic" scattering case

$$|f(\theta,\phi)||\Lambda(k\sin\theta\cos\phi)||\Lambda(k\sin\theta\sin\phi)| = \text{constant} \tag{11}$$

which yields

$$\max_{\theta,\phi} D(\theta,\phi) = 2 \tag{12}$$

We can therefore define an "absolute" lower bound for the RCS ratio as

$$\gamma_{\text{abs}} \approx \frac{1}{2\pi}\left(\frac{\lambda}{Nd}\right)^2 = \frac{\lambda^2}{2\pi A} \tag{13}$$

Such scaling law is also shown (magenta-dashed dotted line) in Figure 2, and its comparison with the optimized coding results seems to indicate, at least in principle, the possibility to uniformly reduce the RCS ratio by ≈12 dB. However, the condition in Equation (11) requires the array factor to perfectly compensate the element factor, which cannot be realistically attained. First, it is clear from Equation (5) that the element factor may exhibit nulls (for $d > \lambda$) that would render the compensation impossible. Moreover, even in the absence of nulls, the spectral shaping that can be synthesized in the array factor by exploiting binary coefficients is quite limited (see, e.g., ref. [42] for one of the very few synthesis approaches available). Overall, the absolute lower bound in Equation (13) is expected to be rather loose.

A more realistic bound can be derived by considering another possible condition that yields a constant directivity, namely an isotropic array factor (IAF),

$$|\Lambda(\kappa)| = \text{constant} \tag{14}$$

In this case, it readily follows from Equation (10) that

$$D(\theta,\phi) \approx \frac{4\pi|f(\theta,\phi)|^2}{\int\limits_{-\pi}^{\pi}d\phi\int\limits_{0}^{\pi/2}d\theta\sin\theta|f(\theta,\phi)|^2} \tag{15}$$

i.e., the metasurface directivity coincides with the supercell directivity. In other words, the metasurface directivity depends solely on the supercell electrical size, but not on the number of supercells (and, hence, on the total size). **Figure 3** shows the maximum value of the supercell directivity in Equation (15) as a function of its electrical size, from which it is evident that the supercell should be made as small as possible. However, there are inherent limitations in the minimum size of the supercell that are intrinsically related to the approximations implied in the semianalytical model. Such model ideally assumes that an arbitrary binary distribution of local reflection coefficients can be induced on the metasurface. However, the physical unit cells are designed via full-wave simulations assuming an infinite periodic structure made of identical ("1" or "0" element type) unit cells. Clearly, the above assumption represents a reasonable approximation as long as each supercell in the metasurface is sufficiently large so as to establish a local periodicity condition, and inevitably breaks down below a critically small size. Intuitively, such critical size is on the order of a wavelength.
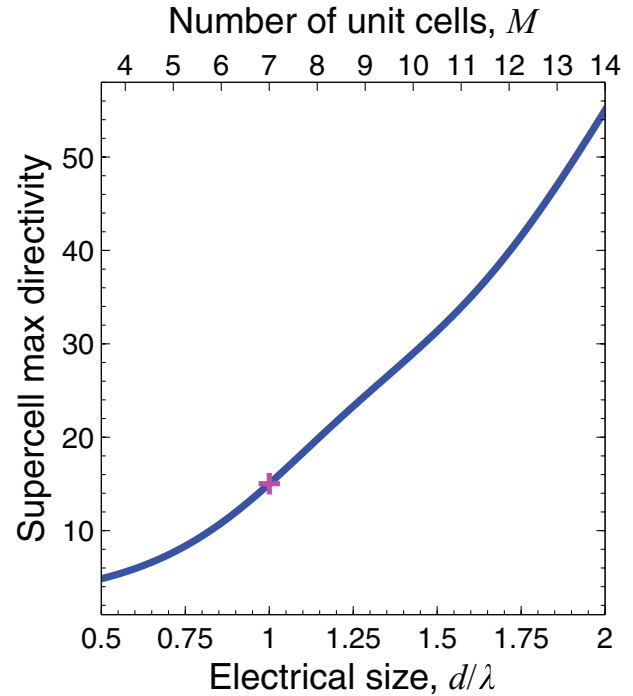
Figure 3. Supercell maximum directivity (Equation (15)) as a function of electrical size. Also indicated (top axis) is the corresponding number M of unit cells (of period $a = \lambda/7$) per linear dimension. The magenta-cross marker indicates the selected parameter configuration ($d = \lambda$, $M = 7$).

Accordingly, we assume a supercell of sidelength $d = \lambda$, comprising 7×7 unit cells, which is also the configuration considered in the optimized-coding results.[10] By extracting from Figure 3 the corresponding maximum directivity (magenta-cross marker), and substituting it in Equation (3), we obtain

$$\gamma_{\text{IAF}} \approx \frac{15.01}{4\pi}\left(\frac{\lambda}{Nd}\right)^2 = \frac{15.01\lambda^2}{4\pi A} \tag{16}$$

henceforth referred to as "IAF bound." Also this scaling law is shown (purple-dashed line) in Figure 2. Remarkably, the IAF bound appears rather close to (≈3 dB below) the optimized-coding results, thereby indicating that the brute-force numerical optimization might be somehow equivalent (in terms of RCS reduction) to "flattening" the array factor response.

3.3. Suboptimal Design

The above analysis suggests a possible "suboptimal" coding strategy based on the IAF condition in Equation (14). It is expedient to recast the array factor in Equation (9) in the canonical polynomial form

$$\Lambda(\xi) = \sum_{n=0}^{N-1}\Gamma_n\xi^n, \quad \Gamma_n \in \{-1,1\} \tag{17}$$

where $\xi = \exp(-i\kappa d)$, and the phase reference has been suitably chosen so as to eliminate an irrelevant phase factor in the Γ_n coefficients. This allows us to directly establish an intriguing

**ADVANCED
SCIENCE NEWS**
www.advancedsciencenews.com

**ADVANCED
OPTICAL
MATERIALS**
www.advopticalmat.de

connection between the IAF condition in Equation (14) and a celebrated problem in pure mathematics that was originally posed by Erdős[43] and Littlewood.[44] The problem concerns to what extent the absolute value of a polynomial as in Equation (17) can be made almost constant on the unit circle or, in mathematical terms

$$|\Lambda(\xi)| = \sqrt{N}, \quad |\xi| = 1 \tag{18}$$

where the constant $\sqrt{N}$ is the root-mean-square value (see Supporting Information for details). Clearly, the strict equality in Equation (18) is impossible for $N > 1$, and suitably weaker metrics should be considered. For instance, the so-called "flatness" condition[44] requires that two constants $0 < C_1 < 1 < C_2$ exist so that

$$C_1\sqrt{N} \le |\Lambda(\xi)| \le C_2\sqrt{N}, \quad |\xi| = 1 \tag{19}$$

A more stringent condition, usually referred to as "ultraflatness,"[44] requires instead the existence of a sequence of polynomials $\{\Lambda_j\}$ (of degree $N_j - 1$) such that

$$\max_{|\xi|=1}\left\| \Lambda_j(\xi) \right| - \sqrt{N_j} \right| \le \eta_j\sqrt{N_j}, \quad \eta_j \to 0 \tag{20}$$

To date, the above problem remains elusive and largely open, with several theoretical results and conjectures available. For instance, it has been proved that a random choice of the coefficients is quite poor in terms of flatness, as it yields (see, e.g., ref. [45])

$$\max_{|\xi|=1}\Lambda(\xi) \sim \sqrt{N\log N} \tag{21}$$

as $N \to \infty$ with probability tending to one. Moreover, it was conjectured by Erdős[43] that

$$\max_{|\xi|=1}\Lambda(\xi) \ge \chi\sqrt{N}, \quad \chi > 1 \tag{22}$$

which would prevent the ultraflatness condition in Equation (20). In fact, if the binary constraint on the Γ_n coefficients is relaxed, e.g., by assuming simple unimodularity ($|\Gamma_n| = 1$), the ultraflatness condition can be attained. This was demonstrated, by using probabilistic arguments, by Kahane[46] and subsequently, in a constructive form, by Bombieri and Bourgain.[47] However, for the binary coding ($\Gamma_n \in \{-1,1\}$) of interest in our study, there is no rigorous proof available. Indeed, for this case, extensive numerical searches[48] suggest the validity of the Erdős conjecture in Equation (22), and the bounding constants $C_1 \approx 0.64$ and $C_2 \approx 1.27$ for the flatness condition in Equation (19).

Among the well-studied cases, particularly appealing are the Barker sequences,[49] which are widely utilized in communications and radar applications. Unfortunately, they can only be constructed for $N = 3, 4, 5, 7, 11, 13$, and it is conjectured that they do not exist for $N > 13$; this renders them of scarce interest for our intended application.

Another very interesting example is provided by the Golay-Rudin-Shapiro (GRS) polynomials,[50–52] which have found interesting applications ranging from antenna arrays[53] to spread-spectrum communications.[54] The P_v and Q_v GRS polynomials can be recursively defined via two intertwined formulas

$$\begin{aligned} P_{v+1}(\xi) &= P_v(\xi) + \xi^{2^v}Q_v(\xi) \\ Q_{v+1}(\xi) &= P_v(\xi) - \xi^{2^v}Q_v(\xi) \end{aligned} \tag{23}$$

with

$$P_0 = Q_0 = 1 \tag{24}$$

It can be verified that these polynomials belong to the general class in Equation (17), with $N = 2^v$. Moreover[52]

$$|P_v(\xi)| \le 2^{\frac{v+1}{2}}, \quad |Q_v(\xi)| \le 2^{\frac{v+1}{2}}, \quad |\xi| = 1 \tag{25}$$

i.e., they satisfy the upper-bound in Equation (19) with $C_2 = \sqrt{2}$. No rigorous theoretical results are instead available for the lower bound. For $N \ne 2^v$, GRS-type sequences can still be constructed, but they are characterized by a looser upper bound[52] $C_2 = 2 + \sqrt{2}$.

With a view toward our IAF-based coding strategy, GRS polynomials seem to constitute a reasonable compromise between "flatness" and simple, deterministic structure. In particular, their algorithmic generation requires negligible computational burden, irrespective of the coding sequence size.

Figure 4 shows the magnitude distributions (over the unit circle) pertaining to three representative orders. A complementary behavior of the P- and Q-types is observed, which can be rigorously expressed as[52]

$$|P_v(\xi)|^2 + |Q_v(\xi)|^2 = 2^{v+1}, \quad |\xi| = 1 \tag{26}$$

Additional theoretical results on their zeros can be found in ref. [55] (see also the Supporting Information).

From the algorithmic viewpoint, the generation of GRS-coded metasurfaces is rather straightforward. For a chosen sequence length and type (P or Q), the coefficients $\Gamma_n \in \{-1, 1\}$ could be directly calculated from the recursive definitions in Equation (23), by using symbolic-manipulation tools. We utilize instead a simpler algorithm,[52] based on the generation of an auxiliary binary sequence with the alphabet $\{-1, 1\}$
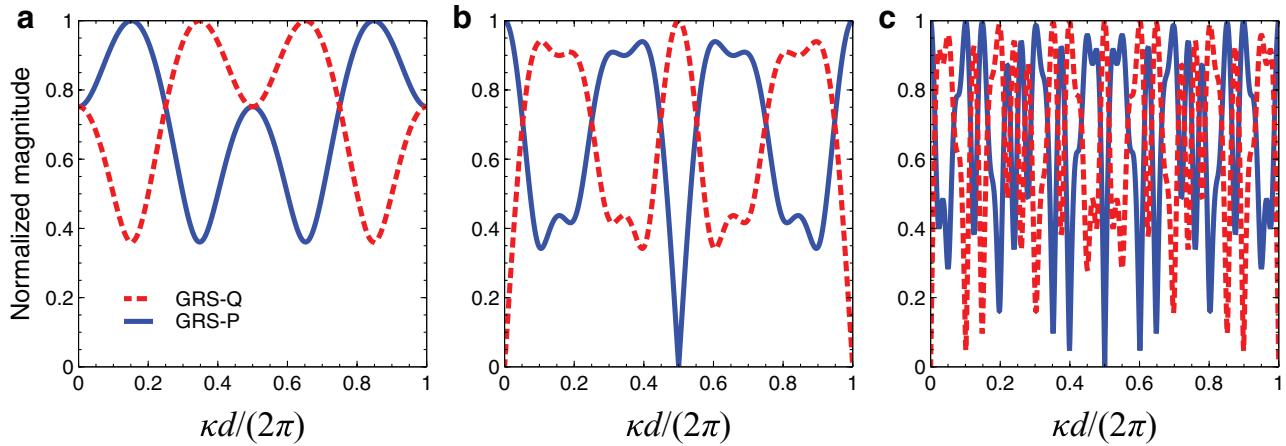
$$\varsigma_0 = 1, \quad \varsigma_{2n} = \varsigma_n, \quad \varsigma_{2n+1} = (-1)^n\varsigma_n \tag{27}$$

which, for $N = 2^v$, directly yields the reflection-coefficient sequence pertaining to the P_v-type polynomials

$$\Gamma_n = \varsigma_n, \quad n = 0,...,N-1 \tag{28}$$

and, with a sign flip in the second half, also yields the sequence pertaining to the Q_v-type polynomials

$$\Gamma_n = \begin{cases} \varsigma_n, & n = 0,...,\dfrac{N}{2}-1 \\ -\varsigma_n, & n = \dfrac{N}{2},...,N-1 \end{cases} \tag{29}$$

**ADVANCED
SCIENCE NEWS**

www.advancedsciencenews.com

**ADVANCED
OPTICAL
MATERIALS**

www.advopticalmat.de

Figure 4. GRS polynomials. a–c) Normalized magnitude of P_ν (blue-solid curves) and Q_ν (red-dashed curves) polynomials, for $\nu = 2, 3, 5$, respectively, with argument running over the unit circle [$\xi = \exp(-i\kappa d)$].

Next, without loss of generality, we associate $\Gamma_n = 1$ with a "1" element-type, and $\Gamma_n = -1$ with a "0" element type. Nevertheless, we stress that, in view of the symmetry in the GRS-polynomial magnitude distributions (cf. Figure 4), the opposite association would yield equivalent results. The GRS coding sequences are explicitly reported in Tables S2 and S3 (Supporting Information) for P_ν and Q_ν polynomials, respectively, with $2 \le \nu \le 7$.

Figure 5 shows the full-wave computed (see the Supporting Information for details) 3-D RCS patterns for representative structures. In particularly, we consider P_ν- and Q_ν-type coding, with $\nu = 3$ (8×8 supercells, i.e., $8\lambda \times 8\lambda$ total size) and $\nu = 4$ (16×16 supercells, i.e., $16\lambda \times 16\lambda$ total size), with same unit-cell, supercell, and operational frequency as for the optimized-coding results in Figure 2. As it can be observed, a diffuse scattering is obtained, with reasonably uniform distributions of lobes.

For a more quantitative assessment, **Figure 6** shows the RCS-ratio scaling laws. More specifically, the semianalytical results are shown for orders up to $\nu = 7$ (corresponding to a maximum total size of $128\lambda \times 128\lambda$), whereas the full-wave results are limited to orders $\nu = 3$ and $\nu = 4$ (cf. Figure 5), which are compatible with our current computational resources. The very good agreement with the full-wave simulations provides an independent validation for the semianalytical modeling, which can therefore be utilized as a reliable prediction tool in the electrically large-size regime where full-wave simulations are computationally unaffordable. The scaling laws exhibit fairly linear trends, with slopes very similar to the IAF bound, and only few dB differences in the intercepts. To give an idea, a Q-type GRS-coded metasurface of size $16\lambda \times 16\lambda$ yields an RCS reduction of ≈19 dB, i.e., only ≈4 dB less than the IAF bound. Such differences are attributable to the imperfect flatness of the GRS polynomials. The algebraic numerical fits yield

$$\gamma_{\mathrm{GRSP}} \approx 4.375 \left(\frac{\lambda}{Nd} \right)^{1.991} \approx \frac{54.98 \lambda^{1.991}}{4\pi A^{0.9955}} \tag{30}$$

and

$$\gamma_{\mathrm{GRSQ}} \approx 2.73 \left(\frac{\lambda}{Nd} \right)^{1.902} \approx \frac{34.22 \lambda^{1.912}}{4\pi A^{0.951}} \tag{31}$$
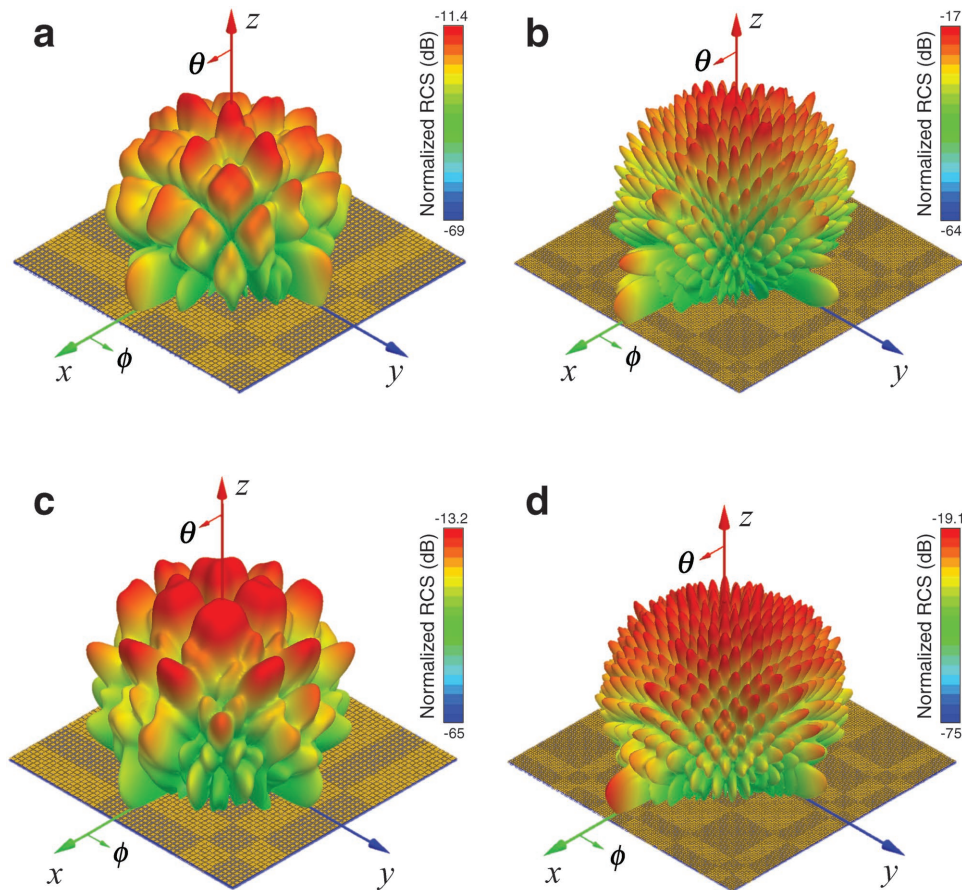
for the P- and Q-type GRS coding, respectively. By comparison with Equation (7), we note that these scaling laws are quantitatively consistent with those pertaining to the optimized coding in ref. [10]. However, unlike brute-force numerical optimization, our proposed synthesis can be inexpensively applied to arbitrarily large sizes.

3.4. Experimental Validation

As a proof-of-concept experimental validation of our proposed GRS-coding design strategy, we fabricated and characterized a metasurface prototype sample operating at microwave frequencies (X-band). Referring to Section 5 for a basic description (and the Supporting Information for more details), we highlight that, for practical fabrication-related reasons, we selected the unit-cell and supercell parameters, as well as the operational frequency, slightly different from the configurations in our numerical study above (see Figure S2 in the Supporting Information for the corresponding phase responses).

Figure 7 illustrates the metasurface design (based on the GSR-P_3 coding) together with a photo of the fabricated prototype. The moderate electrical size ($8\lambda \times 8\lambda$) is dictated by the size of the experimental facility, in order to fulfill the Fraunhofer-condition ensuring a quasi-plane-wave illumination of the target (see the Supporting Information for more details).

Figure 8 compares the full-wave-computed and measured results. More specifically, Figure 8a shows the simulated 3-D RCS pattern (as in Figure 5, but for the assumed prototype parameters and operational frequency). Figure 8b compares the simulated and measured RCS patterns in the $\phi = 0$ plane, showing a fairly good agreement. Finally, for a better illustration of the RCS reduction, Figure 8c,d show the comparisons (simulated and measured, respectively) with a metallic reference target with same size. In the $\phi = 0$ plane, an RCS reduction of ≈11.6 dB is experimentally observed, which is in line with the numerical estimate computed over all possible directions (9.4 dB, cf. Figure 8a). We point out that the RCS measurements are carried out at various frequencies, and the best agreement with the simulations is observed at 10.5 GHz. Such

**ADVANCED
SCIENCE NEWS**
www.advancedsciencenews.com

**ADVANCED
OPTICAL
MATERIALS**
www.advopticalmat.de

Figure 5. RCS patterns for GRS-coded metasurfaces. a,b) Full-wave-computed 3-D RCS patterns pertaining to P_3 and P_4 coding, respectively, super-posed on the corresponding metasurface patterns (not in scale). Results are normalized with respect to the maximum RCS of a PEC target of same size. c,d) Same as above, but for Q_3 and Q_4 coding, respectively. The coding sequences are explicitly given in Tables S2 and S3 (Supporting Information). Unit-cell geometry and parameters, as well as supercell size and operational frequency, are as in Figure 2.

slight difference from the nominal design frequency (10 GHz) was also observed in previous experimental studies[31] relying on the same fabrication process, and may thus be attributable to fabrication tolerances as well as uncertainty on the substrate parameters. Similar frequency shifts were also observed for THz experiments.[56] Overall, the above characterization demonstrates the practical viability of the proposed coding strategy, and validates the theoretical and numerical predictions of our study.

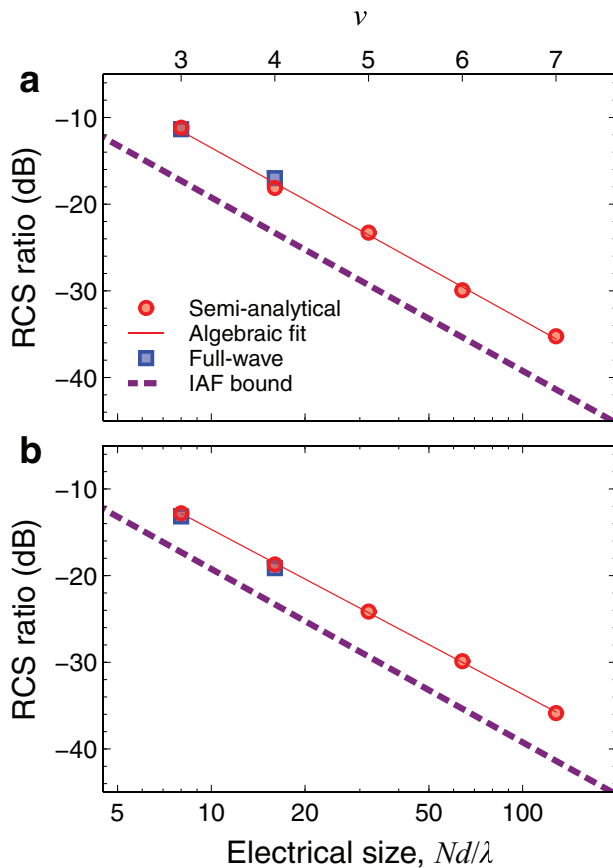### 3.5. Frequency and Angular Stability

The results in our study are obtained assuming a fixed frequency and normally incident plane-wave illumination. One might wonder to what extent they are robust with respect to frequency and/or incidence variations. Remarkably, our suboptimal coding design is independent of frequency and incidence conditions, as long as the "1" and "0" element-types maintain the out-of-phase responses. In this case, in our semianalytical model, frequency and incidence variations translate into spectral scaling and shifts, respectively, in the array-factor in Equation (6). However, given the flat spectral character implied

by our suboptimal coding, it is easily understood that scaling and shifts do not yield sensible effects in the (maximum) RCS response. Therefore, the robustness is essentially dictated by the element design. Within this framework, we stress that the element design was not the focus of this study, and that a simple patch-type design was chosen, mainly to facilitate direct comparison with previous studies.[10] Nevertheless, we show in the Supporting Information some representative results (Figures S3–S5, Supporting Information) that indicate a reasonable stability for variations of the frequency and incidence variations. Clearly, different element-types could be considered, with optimized stability with respect to frequency and incidence conditions (see, e.g., ref. [17]).

3.6. Some Remarks

As previously mentioned, GRS polynomials provide a reasonable tradeoff between simplicity of design and performance. Nevertheless, one might wonder to what extent the uniformity of the scattered field can be improved. Although no rigorous theoretical results are available in this respect, the aforementioned numerical estimates[48] of the bounding

**ADVANCED
SCIENCE NEWS**

www.advancedsciencenews.com

**ADVANCED
OPTICAL
MATERIALS**

www.advopticalmat.de

Figure 6. RCS-ratio scaling-laws for GRS-coded metasurfaces. a) RCS ratio computed via the semianalytical model (red-circle markers) and full-wave simulations (blue-square markers) pertaining to P_v-type as a function of the metasurface electrical size on a log–log scale. The corresponding order v is shown on the top axis. Also shown, as references, are the algebraic fit of the semianalytical results (Equation (30); red-solid line) and the IAF bound (Equation (16); purple-dashed line). b) Same as above, but for Q_v-type; the corresponding algebraic fit of the semianalytical results is given in Equation (31). The coding sequences are explicitly given in Tables S2 and S3 (Supporting Information). Unit-cell geometry and parameters, as well as supercell size and operational frequency, are as in Figure 2.

constants ($C_1 \approx 0.64$ and $C_2 \approx 1.27$) for the flatness condition in Equation (19) suggest that no significant improvements should be expected for binary codings. Conversely, by relaxing the binary constraints, the ultraflatness condition in Equation (20) can be in principle approached, which should result in more uniform scattering patterns. The reader is referred to ref. [57] for examples of polynomials with polyphase coefficients, characterized by particularly uniform magnitude distributions. Therefore, multi-bit codings should allow some improvement in the scattering-pattern uniformity, at the expense of a more complicated design and implementation.

Another largely open issue is the possibility to extend our results to other applications, rather than RCS reduction. This would entail, for instance, the capability of shaping the array factor in more general ways. Once again, as previously mentioned, the binary-coding constraint poses significant limitations on the spectral shaping that can be synthesized.

Nevertheless, there are some synthesis approaches available in the literature that could be explored. For instance, in ref. [42], an approach based on Markov chains is proposed that allows some limited spectral-shaping capabilities.

4. Conclusions

In conclusion, we have investigated the design of coding metasurfaces for diffuse scattering. The main outcomes of this study can be summarized as follows. By analyzing the scaling-laws of the RCS ratio (with reference to a metallic scatterer of same size) attained via numerically optimized coding, we have elucidated their basic working principle, which essentially consists of maintaining the metasurface directivity independent of its electrical size. This observation suggests the theoretical derivation of a realistic bound to the RCS reduction, which exhibits a similar scaling law as the optimized coding. Moreover, it also establishes an intriguing connection with the problem of "flat polynomials" in pure mathematics, from which a simple, deterministic suboptimal design strategy can be borrowed. This turns out to yield RCS-ratio scaling laws that are in line with those exhibited by the numerically optimized coding considered in our study, while requiring a negligible computational burden, irrespective of the metasurface electrical size.

The above results and predictions rely on semianalytical modeling, full-wave numerical simulations and microwave (X-band) measurements, which have been cross-validated. They provide some rigorous grounds and effective design tools for coding metasurfaces, which can also be extended to THz and optical frequencies, as well as to other physical domains (e.g., acoustics). Within this framework, the fabrication and experimental characterization of THz samples is currently under way and will be the subject of a forthcoming paper. Also of great interest are possible extensions to multi-bit coding, which would provide more flexibility in terms of array-factor shaping. This may enable to approach the absolute lower bound for RCS reduction, and may also find more general applications to complex field shaping as well as computational imaging.

5. Experimental Section

For experimental confirmation, a microwave (X-band) prototype of a coding metasurface was fabricated, with a nominal working frequency of 10 GHz. A standard printed-circuit-board fabrication process was employed, by utilizing a commercial FR4 substrate with nominal relative permittivity $\varepsilon_r = 4.3$, tangent loss $\tan \delta = 0.03$, thickness $h = 1.6$ mm, and copper metallization of thickness 18 μm. The prototype (shown in Figure 7b) comprised 8×8 supercells of sidelength $d = 28$ mm (each consisting of 4×4 unit cells of period $a = 7$ mm), resulting in a total area of 224×224 mm^2. The patch sidelengths pertaining to the "1" and "0" element-types are $w_1 = 5$ mm and $w_0 = 6.5$ mm, respectively (see Figure 1d). A representative sub-optimal coding was implemented.

The experimental characterization was carried out by measuring the bistatic RCS of the metasurface prototype (as well as that of a reference copper plate of same size) by means of a dedicated indoor measurement setup comprising an anechoic chamber, transmitting and receiving horn antennas, vector network analyzer, rotary support, and personal computer with GPIB interface (see Figure S6 in the Supporting Information). The far-field radiation pattern is obtained
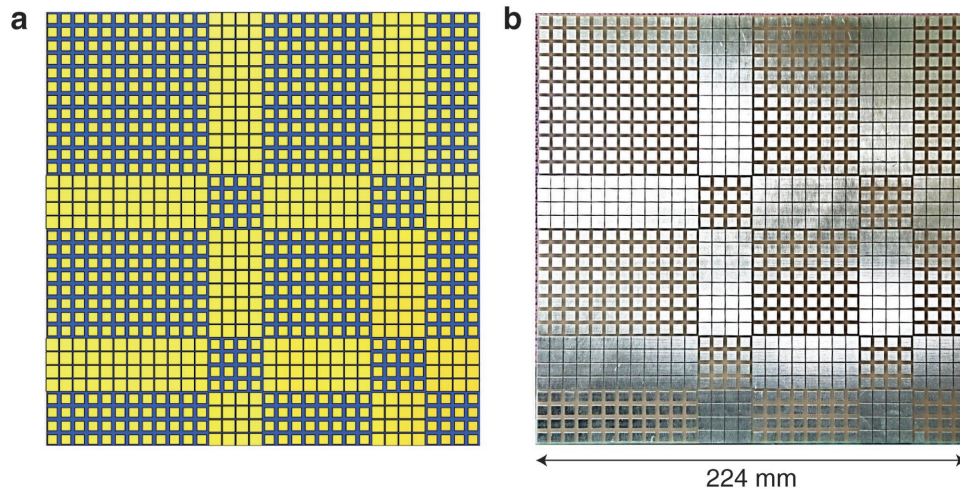
Figure 7. Prototype design and fabrication. a) Metasurface design pertaining to a GRS-P$_3$ coding. The design assumes an FR4 substrate ($\varepsilon_r = 4.3$, tan $\delta = 0.03$, $h = 1.6$ mm, and copper metallization of thickness 18 μm), and comprises 8 × 8 supercells of sidelength $d = 28$ mm (each consisting of 4 × 4 unit cells of period $a = 7$ mm), resulting in a total area of 224 × 224 mm^2. The patch sidelengths pertaining to the "1" and "0" element-types are $w_1 = 5$ mm and $w_0 = 6.5$ mm, respectively (see Figure 1d). The nominal operational frequency is 10 GHz. b) Photo of fabricated prototype.
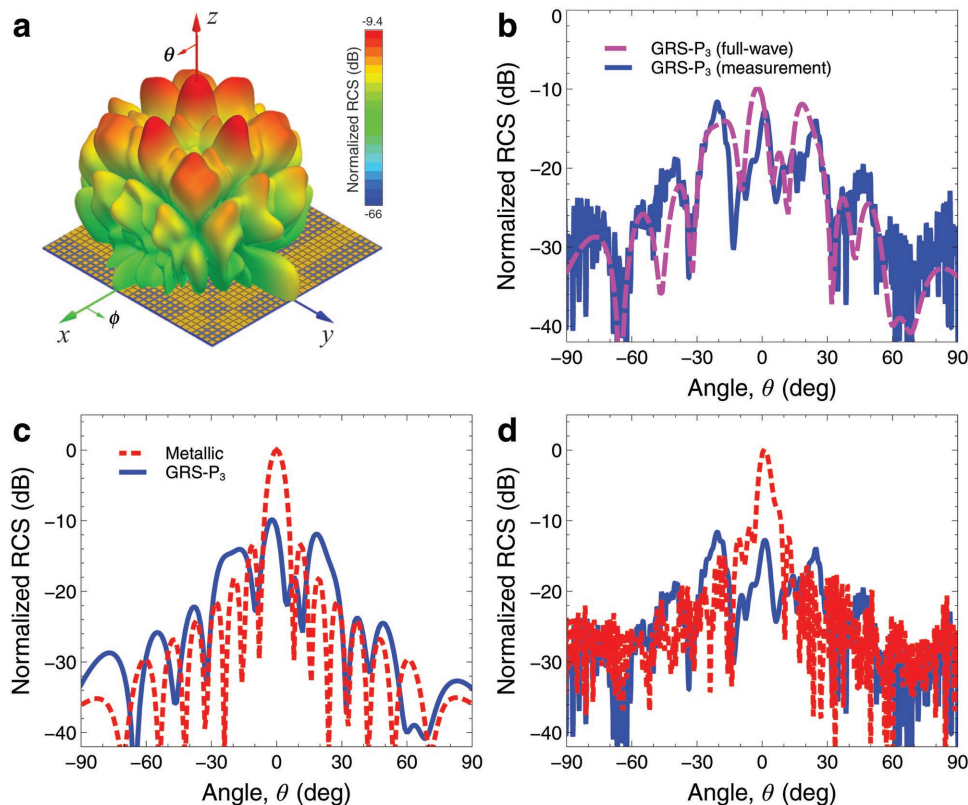
Figure 8. Experimental validation. a) Full-wave-computed 3-D RCS pattern pertaining to the prototype in Figure 7, superposed on the corresponding metasurface pattern. Results are normalized with respect to the maximum RCS of a PEC target of same size. b) Full-wave-computed (magenta-dashed curve) and measured (blue-solid curve) RCS pattern cut (in the $\phi = 0$ plane). c,d) Full-wave-computed and measured, respectively, RCS pattern cuts (in the $\phi = 0$ plane) pertaining to the metasurface prototype (blue-solid curves) and a metallic reference scatterer of same size (red-dashed curves). Results in panels (b–d) are normalized with respect to the maximum RCS of the metallic scatterer (at $\theta = 0$). Simulated and measured results pertain to slightly different operational frequencies (10 GHz and 10.5 GHz, respectively).

when the rotatory support, carrying both the transmitting antenna and metasurface, automatically rotates 360° in the horizontal plane.

Further details can be found in the Supporting Information.

Supporting Information

Supporting Information is available from the Wiley Online Library or from the author.

Conflict of Interest

The authors declare no conflict of interest.

Keywords

coding, digital, diffuse scattering, flat polynomials, metasurfaces

[1] N. Yu, P. Genevet, M. A. Kats, F. Aieta, J.-P. Tetienne, F. Capasso, Z. Gaburro, *Science* **2011**, *334*, 333.

[2] W. Kennedy, D. Berry, R. Malech, *IEEE Trans. Antennas Propag.* **1963**, *11*, 645.

[3] D. McGrath, *IEEE Trans. Antennas Propag.* **1986**, *34*, 46.

[4] F. Capolino, *Theory and Phenomena of Metamaterials*, CRC Press, Boca Raton, FL, USA **2009**.

[5] N. Yu, F. Capasso, *Nat. Mater.* **2014**, *13*, 139.

[6] Y. Zhao, X.-X. Liu, A. Alù, *J. Opt.* **2014**, *16*, 1.

[7] N. Yu, F. Capasso, *J. Lightwave Technol.* **2015**, *33*, 2344.

[8] N. M. Estakhri, A. Alù, *J. Opt. Soc. Am. B* **2016**, *33*, A21.

[9] H.-T. Chen, A. J. Taylor, N. Yu, *Rep. Prog. Phys.* **2016**, *79*, 1.

[10] T. J. Cui, M. Q. Qi, X. Wan, J. Zhao, Q. Cheng, *Light Sci. Appl.* **2014**, *3*, e218.

[11] C. D. Giovampaola, N. Engheta, *Nat. Mater.* **2014**, *13*, 1115.

[12] M. Paquay, J.-C. Iriarte, I. Ederra, R. Gonzalo, P. de Maagt, *IEEE Trans. Antennas Propag.* **2007**, *55*, 3630.

[13] S. Simms, V. Fusco, *Electron. Lett.* **2008**, *44*, 316.

[14] V. Galdi, V. Pierro, G. Castaldi, N. Engheta, *IEEE Antennas Wireless Propag. Lett.* **2008**, *7*, 788.

[15] Y. Zhang, R. Mittra, B. Z. Wang, N. T. Huang, *Electron. Lett.* **2009**, *45*, 484.

[16] Y. Fu, Y. Li, N. Yuan, *Microw. Opt. Technol. Lett.* **2011**, *53*, 712.

[17] A. Edalati, K. Sarabandi, *IEEE Trans. Antennas Propag.* **2014**, *62*, 747.

[18] W. Chen, C. A. Balanis, C. R. Birtcher, *IEEE Trans. Antennas Propag.* **2015**, *63*, 2636.

[19] N. Kaina, M. Dupré, G. Lerosey, M. Fink, *Sci. Rep.* **2014**, *4*, 6693.

[20] K. Wang, J. Zhao, Q. Cheng, D. S. Dong, T. J. Cui, *Sci. Rep.* **2014**, *4*, 5935.

[21] X. Yan, L. Liang, J. Yang, W. Liu, X. Ding, D. Xu, Y. Zhang, T. Cui, J. Yao, *Opt. Express* **2015**, *23*, 29128.

[22] L.-H. Gao, Q. Cheng, J. Yang, S.-J. Ma, J. Zhao, S. Liu, H.-B. Chen, Q. He, W. X. Jiang, H. F. Ma, Q.-Y. Wen, L.-J. Liang, B.-B. Jin, W.-W. Liu, L. Zhou, J.-Q. Yao, P.-H. Wu, T. J. Cui, *Light Sci. Appl.* **2015**, *4*, e324.

[23] D. S. Dong, J. Yang, Q. Cheng, J. Zhao, L.-H. Gao, S.-J. Ma, S. Liu, H. B. Chen, Q. He, W.-W. Liu, Z. Fang, L. Zhou, T. J. Cui, *Adv. Opt. Mater.* **2015**, *3*, 1405.

[24] S. Liu, T. J. Cui, Q. Xu, D. Bao, L. Du, X. Wan, W. X. Tang, C. Ouyang, X. Y. Zhou, H. Yuan, H. F. Ma, W. X. Jiang, J. Han, W. Zhang, Q. Cheng, *Light Sci. Appl.* **2016**, *5*, e16076.

[25] P. Su, Y. Zhao, S. Jia, W. Shi, H. Wang, *Sci. Rep.* **2016**, *6*, 20387.

[26] Y. B. Li, L. L. Li, B. B. Xu, W. Wu, R. Y. Wu, X. Wan, Q. Cheng, T. J. Cui, *Sci. Rep.* **2016**, *6*, 23731.

[27] Y. Zhao, X. Cao, J. Gao, Y. Sun, H. Yang, X. Liu, Y. Zhou, T. Han, W. Chen, *Sci. Rep.* **2016**, *6*, 23896.

[28] W. Pan, C. Huang, M. Pu, X. Ma, J. Cui, B. Zhao, X. Luo, *Sci. Rep.* **2016**, *6*, 21462.

[29] Y. Zhao, X. Cao, J. Gao, X. Liu, S. Li, *Opt. Express* **2016**, *24*, 11208.

[30] Y. Zhang, L. Liang, J. Yang, Y. Feng, B. Zhu, J. Zhao, T. Jiang, B. Jin, W. Liu, *Sci. Rep.* **2016**, *6*, 26875.

[31] T. J. Cui, S. Liu, L. L. Li, *Light Sci. Appl.* **2016**, *5*, e16172.

[32] Z. Shen, B. Jin, J. Zhao, Y. Feng, L. Kang, W. Xu, J. Chen, P. Wu, *Appl. Phys. Lett.* **2016**, *109*, 121103.

[33] H. Yang, X. Cao, F. Yang, J. Gao, S. Xu, M. Li, X. Chen, Y. Zhao, Y. Zheng, S. Li, *Sci. Rep.* **2016**, *6*, 35692.

[34] K. Chen, Y. Feng, Z. Yang, L. Cui, J. Zhao, B. Zhu, T. Jiang, *Sci. Rep.* **2016**, *6*, 35968.

[35] S. J. Li, X. Y. Cao, L. M. Xu, L. J. Zhou, H. H. Yang, J. F. Han, Z. Zhang, D. Zhang, X. Liu, C. Zhang, Y. J. Zheng, Y. Zhao, *Sci. Rep.* **2016**, *5*, 37409.

[36] S. Liu, T. J. Cui, *Sci. Rep.* **2016**, *6*, 37545.

[37] L. Liang, M. Wei, X. Yan, D. Wei, D. Liang, J. Han, X. Ding, G. Zhang, J. Yao, *Sci. Rep.* **2016**, *6*, 39252.

[38] J. Zhao, Q. Cheng, X. K. Wang, M. J. Yuan, X. Zhou, X. J. Fu, M. Q. Qi, S. Liu, H. B. Chen, Y. Zhang, T. J. Cui, *Adv. Opt. Mater.* **2016**, *4*, 1773.

[39] B. Xie, K. Tang, H. Cheng, Z. Liu, S. Chen, J. Tian, *Adv. Mater.* **2017**, *29*, 1603507.

[40] B. Xie, H. Cheng, K. Tang, Z. Liu, S. Chen, J. Tian, *Phys. Rev. Appl.* **2017**, *7*, 024010.

[41] R. E. Collin, *Antennas and Radiowave Propagation*, McGraw-Hill College, New York **1985**.

[42] A. Harms, W. U. Bajway, R. Calderbankz, in *Proc. IEEE 5th Int. Workshop on Computational Advances in Multi-Sensor Adaptive Processing (CAMSAP)*, IEEE, Piscataway, NJ, USA **2013**, p. 236.

[43] P. Erdős, *Mich. Math. J.* **1957**, *4*, 291.

[44] J. E. Littlewood, *J. London Math. Soc.* **1966**, *41*, 336.

[45] A. Gersho, B. Gopinath, A. M. Odlyzko, *Bell Syst. Tech. J.* **1979**, *58*, 2301.

[46] J. P. Kahane, *Bull. London Math. Soc.* **1980**, *12*, 321.

[47] E. Bombieri, J. Bourgain, *J. Eur. Math. Soc.* **2009**, *11*, 627.

[48] A. Odlyzko, *Search for ultraflat polynomials with plus and minus one coefficients*, http://www.dtc.umn.edu/~odlyzko/doc/ultraflat.pdf (accessed: May 2017).

[49] S. W. Golomb, G. Gong, *Signal Design for Good Correlation: for Wireless Communication, Cryptography, and Radar*, Cambridge University Press, Cambridge, UK **2005**.

[50] M. J. E. Golay, *J. Opt. Soc. Am.* **1951**, *41*, 468.

[51] H. S. Shapiro, *M.S. Thesis*, Massachusetts Institute of Technology, **1952**.

[52] W. Rudin, *Proc. Am. Math. Soc.* **1959**, *10*, 855.

[53] V. Galdi, V. Pierro, G. Castaldi, I. M. Pinto, L. B. Felsen, *IEEE Trans. Antennas Propag.* **2005**, *53*, 3568.

[54] A. la Cour-Harbo, *Appl. Comp. Harm. Anal.* **2008**, *24*, 310.

[55] J. Brillhart, *Duke Math. J.* **1973**, *40*, 335.

[56] S. Liu, T. J. Cui, L. Zhang, Q. Xu, Q. Wang, X. Wan, J. Q. Gu, W. X. Tang, M. Qing Qi, J. G. Han, W. L. Zhang, X. Y. Zhou, Q. Cheng, *Adv. Sci.* **2016**, *3*, 1600156.

[57] P. Borwein, R. Ferguson, J. Knauer, in Number Theory and Polynomials, *London Mathematical Society Lecture Note Series*, Vol. *352* (Eds: J. McKee, C. Smyth), Cambridge University Press, Cambridge, UK **2008**.